Nanoscale

ROYAL SOCIETY
OF **CHEMISTRY**

PAPER
Guan-Jun Yang *et al.*
Small molecule-driven directional movement enabling pin-hole free
perovskite film *via* fast solution engineering

NCNST

Small molecule-driven directional movement enabling pin-hole free perovskite film *via* fast solution engineering†

Li-Li Gao, Ke-Jie Zhang, (ID) Lin Chen, Ni Chen, Cheng-Xin Li, Chang-Jiu Li and Guan-Jun Yang (ID) *

Organolead trihalide perovskite materials have been widely used as light absorbers in efficient photovoltaic cells. Solution engineering is a fast and effective method to fabricate perovskite films. Here, we report a fast precipitation of a pin-hole free perovskite film by small molecule-driven directed diffusion engineering. Solvent molecules diffuse easily and quickly by colliding with small molecules, *e.g.* helium. Fully compact perovskite films and highly efficient perovskite solar cells are achieved, and the devices show remarkable stability of *ca.* 90% original efficiency after more than 1000 hours of testing. The small molecule driving directed diffusion offers a promising fast precipitation of a perovskite film and highly efficient, stable perovskite solar cells.

Introduction

Low-cost organometal halide perovskite solar cells have emerged as a candidate to meet future energy generation demands because a power conversion efficiency (PCE) of more than 20% can be obtained only by simple solution-based processing.[1–5] The rapid increase in perovskite solar cell efficiencies is due to strong optical absorption, long diffusion lengths, and solution process ability enabled by the relatively benign nature of intrinsic defects.[6–10] Moreover, the wide, tunable bandgap properties of perovskite materials are highly attractive for use in multi-junction solar cells on top of narrower bandgap absorbers such as silicon, copper indium gallium selenide and Sn-containing perovskite.[11–14] This presents a pathway to achieving the goal of perovskite solar cell industrialization.

Perovskite film precipitation is the key technology for perovskite solar cell fabrication.[15–18] Many well-established "solvent engineering" methods have achieved a compact pin-hole free perovskite film with excellent optical and transport properties.[19–24] Among them, the air-assisted drying perovskite film method is an effective morphology controlling process, which significantly contributes to fast precipitation of the perovskite leading to a very uniform perovskite layer with high surface coverage.[19,25–32] Therefore, it is a prospective method for industrial preparation of large area perovskite films, and the processing parameters, such as air flow and temperature, have been widely investigated.[19,29,33] Apparently, solvent evaporation is the critical step for fast perovskite precipitation. Based on fluid mechanics,[34] there is a boundary layer at the interface of the air flow and solution film surface. Air velocity within the boundary layer is much lower, nearly static. The gaseous solution molecules must pass through the entire boundary layer by diffusion to get away from the liquid interface. However, the diffusion of evaporated solution molecules in the boundary layer is difficult and slow without any external motivation. Therefore, how to tailor diffusion in the boundary layer is of great importance for solvent evaporation processing. Actually, the gaseous solvent molecules (SMs) move in the boundary layer by continuous collision with gas molecules (GMs), leading to extremely roundabout paths. It clearly indicates that the collision between SMs and GMs slows the diffusion of SMs and is therefore the key to tailoring film structures. Apparently, the collision during the diffusion process is mainly attributed to the thermal motion of gaseous molecules, which is extremely complex, irregular and of high frequency (10^9 s^{-1}). The route of thermal motion of gaseous molecules is exceptionally random. As a result, the vast majority of the evaporated gaseous solvent molecules are collided back to the liquid surface, and only a small number of molecules successfully escape away from the boundary layer achieving the net evaporation.

In this study, we report a small molecule-driven preferred diffusion movement to promote the diffusion of SMs in the

State Key Laboratory for Mechanical Behavior of Materials, School of Materials Science and Engineering, Xi'an Jiaotong University, Xi'an, Shaanxi 710049, PR China. E-mail: ygj@mail.xjtu.edu.cn

boundary layer. The collision between solvent molecules and different gas molecules, *i.e.* nitrogen (N_2) and helium (He), is different and rarely concerned. When SMs collide with nitrogen molecules, the collision times are relatively high; however, the number of SMs that cross the boundary layer is low. However, when SMs collide with small helium molecules, the collision times are lower than when colliding with nitrogen molecules, and the probability of SMs crossing the helium boundary layer is nearly four times that of SMs crossing the nitrogen boundary layer based on our simulation statistical analysis. The collision of SMs and helium in the boundary layer is simple and directed, which diffuse outside the boundary layer. The directed collision promotes the diffusion of SMs in the boundary layer. Thereby, drying a thin solution perovskite film by helium is much faster compared to nitrogen and has a much lower usage amount. Experimental results illustrate that a perovskite film presents a more compact morphology when dried by helium compared to nitrogen. The efficiency of a perovskite solar cell that employs film drying by helium is up to 18.44%, and the non-encapsulated solar cell stability can be more than 1000 hours with 90% original efficiency.

Experiments

Materials preparation

Iodine methylamine (CH_3NH_3I), lead iodide (PbI_2, 99.99%), and 2,20,7,70-tetrakis(*N*,*N*-di-*p*-methoxyphenylamine)-9,9-spiro-obifluorene (spiro-OMeTAD) were purchased from Xi'an Polymer Light Technology Corp. Titanium dioxide precursor solvent was synthesized following the reported procedure. *N*,*N*-Dimethylformamide (DMF, 99.8%) was purchased from Sinopharm Chemical Reagent Co., Ltd. All materials were used as received.

Perovskite film and device fabrication

FTO glasses (Pilkington, 15 Ω sq^{-1}) were cleaned with acetone, ethyl alcohol, and deionized water, successively, in an ultrasonic bath for 20 min; then, dried with nitrogen and later treated with ozone and ultraviolet light for 15 min. Subsequently, a compact TiO_2 layer was prepared. The precursor of TiO_2 was prepared according to a previous report.[35] Titanium(IV) isopropoxide (Ti[OCH(CH$_3$)$_2$]$_4$, Aldrich, 99.999%, 2 mL) was mixed with ethanolamine ($H_2NCH_2CH_2OH$, Alfa Aesar, 98+%, 1 mL) and 2-methoxyethanol ($CH_3OCH_2CH_2OH$, Alfa Aesar, 99%, 10 mL), then stirred at 80 °C for 2 h. After cooling to room temperature, the TiO_2 precursor was deposited on FTO substrates by spin coating at 4500 rpm for 30 s and sintered at 80 °C for 10 min and 500 °C for 30 min, forming a compact layer with ~50 nm thickness. A dense perovskite film was prepared by the Multi-flow Air Knife (MAK) method on the TiO_2 layer. Perovskite precursor was composed of PbI_2 and CH_3NH_3I, which were dissolved in a DMF solvent at a molar ratio of 1 : 1 (40 wt%) and stirred at room temperature for 12 h. An appropriate 25 μL of perovskite precursor

solution was dropped on the TiO_2-coated FTO surface and spun at 5000 rpm for 5 s; a faint yellow liquid perovskite precursor film of ~2 μm thickness was obtained. Subsequently, the solution films were quickly dried by nitrogen and helium at different air flow. Then, the dried films were annealed at 100 °C on a hotplate for 10 min. All the abovementioned steps were conducted under ambient conditions at a temperature of 20 ± 3 °C and humidity of 30% ± 5%. About 25 μL spiro-OMeTAD solution was spin coated on perovskite films at 3000 rpm for 30 s. Finally, a Au layer was deposited by thermal evaporation to complete the device fabrication.

Measurement and characterization

The morphologies of the perovskite films were examined by scanning electron microscopy (SEM, VEGA II-XMU, TESCAN, Czech Republic) and atomic force microscopy (AFM, Veeco diInnova, Bruker, America). *J–V* curves of the perovskite solar cells were measured by a Keithley 2400 source-measure unit under the illumination of simulated sunlight, provided by a 450 W Class AAA solar simulator equipped with a filtered Xe lamp, (AM 1.5G, 100 mW cm^{-2}, Sol3A, Oriel Instruments). The output light intensity was calibrated using a single-crystal silicon photovoltaic cell as the reference (91150V, Oriel Instruments). The cells were measured with a non-reflective metal mask covering areas of 0.1 cm^2 to receive sunlight and avoid light scattering through the edges.

Results and discussion

Small molecules driven directed diffusion movement in the helium boundary layer

Based on fluid mechanics theory,[36,37] a boundary layer forms when air flow sweeps the liquid film surface because of viscidity and friction. The transverse fluid velocity in the boundary layer is much lower than that in the mainstream, and the vertical velocity is nearly zero in the lamellar flow. During evaporation processing, the solvent molecules generally undergo the following three stages. First, solvent molecules conquer the molecules' binding force in the liquid surface and enter the boundary layer, as shown in Fig. 1a-I. Second, the gas SMs cross the boundary layer by repeatedly colliding with the GMs, as shown in Fig. 1a-II. Third, SMs enter the mainstream and are quickly taken away by high speed air flow, completing a solvent molecule evaporation process, as shown in Fig. 1a-III. In the entire evaporation process, the diffusion of SMs along the thickness direction of the boundary layer is the slowest, thereby becoming the controlling step. However, SMs' diffusion in the boundary layer is fulfilled by repeatedly colliding with GMs. Therefore, accelerating the vertical collision will significantly promote solvent evaporation.

Apparently, the collision between SMs and GMs in the boundary layer is random. However, no matter how complex the collision is, the final collision result is nothing but two types: one is that SMs cross the boundary layer and another result is that SMs return back to the liquid surface, as shown
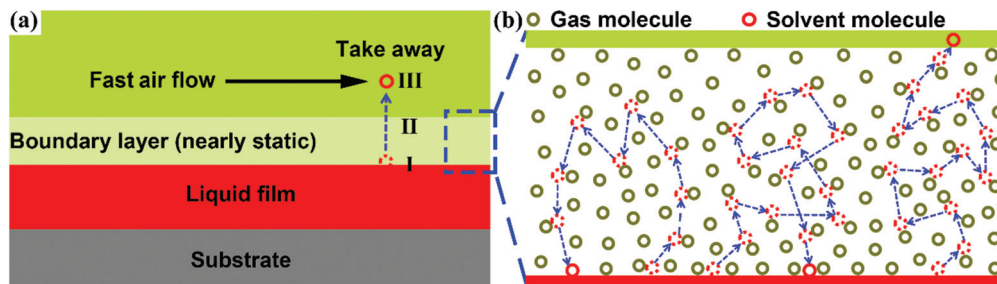
Fig. 1 Schematic of (a) the structure distribution of air flow and the liquid film and (b) the solvent molecule's diffusion in the boundary layer.

in Fig. 1b. It is well known that a bullet can fly in a straight line without changing route because of the tremendous density difference between the bullet and the air molecules. Similarly, air molecules colliding with the bullet has almost no effect on bullet's route because the force resulting from the collision of air molecules is much lower than the bullet inertia force, as shown in Fig. 2a. Based on this inspiration, we conducted a SM collision with another type of GM, which is much lighter in mass and smaller in size than that of the SMs. In this manuscript, we choose DMF as the SM and helium as the lighter and smaller GM, which can be compared with conventionally used nitrogen. As a result, the collision conditions were much different, as shown in Fig. 2b and c. The route of SMs colliding with nitrogen is tortuous (Fig. 2b), while being quite direct with helium (Fig. 2c).

To investigate the collision between SMs and two types of GMs in the boundary layer, Monte Carlo simulation was performed. DMF molecules are SMs, whereas helium and nitro-

gen molecules are GMs. The collision occurs vertically in the boundary layer. The simulation conditions and process are illustrated in ESI:† the relevant parameters are calculated and shown in Tables S1 and S2† and the simulation model is also shown in Fig. S1.† First, we record the collision route of nitrogen and helium molecules, as shown in Fig. 3a and b. The collision route in the nitrogen boundary layer is complex and circuitous. It needs to collide seven hundred thousand times to cross the nitrogen boundary layer, of which the thickness is 70 μm (the boundary layer of nitrogen and helium are calculated, as shown in ESI;† at the same conditions, the nitrogen boundary layer is 70 μm, while the helium boundary layer is a much larger (120 μm) because of the much smaller density). The collision between the nitrogen molecule and the SM is complicated, resulting in SM movement without direction. This indicates that SMs need to collide many times to cross the nitrogen boundary layer, whereas the collision route in the helium boundary layer is clear and direct and the number of collisions is only sixty thousand. In addition, the helium boundary layer is 120 μm, which is much thicker than the nitrogen boundary layer. However, the solvent molecules take a relatively straightforward path to escape the helium boundary layer compared to the nitrogen boundary layer. In order to have an intuitive comparison about the collision in the helium and nitrogen boundary layers, videos were made, as shown in ESI† (because of the limitation in showing time, the video of the collision with helium is recorded every 250 collision times and 1500 collision times with nitrogen due to the long showing time). The colliding between small helium molecules and SMs is slight, resulting in SM movement directly out of the boundary layer. Thereby, the collision times are much lower.

We made 5×10^5 SM evaporations from the liquid film surface, and statistically counted the number of SMs that successfully crossed the boundary layer. Every SM experienced frequent collision with GMs. As shown in Fig. 3c, the collision times in the nitrogen boundary layer is widely distributed from dozens to nine hundred thousand. In the helium boundary layer, the collision times mainly concentrate on 100 to 300 thousand. This illustrates that the SM collision times are much lower in the thicker helium boundary layer than in the thinner nitrogen boundary layer. Moreover, the total number of SMs crossing the boundary layer is also counted, as shown
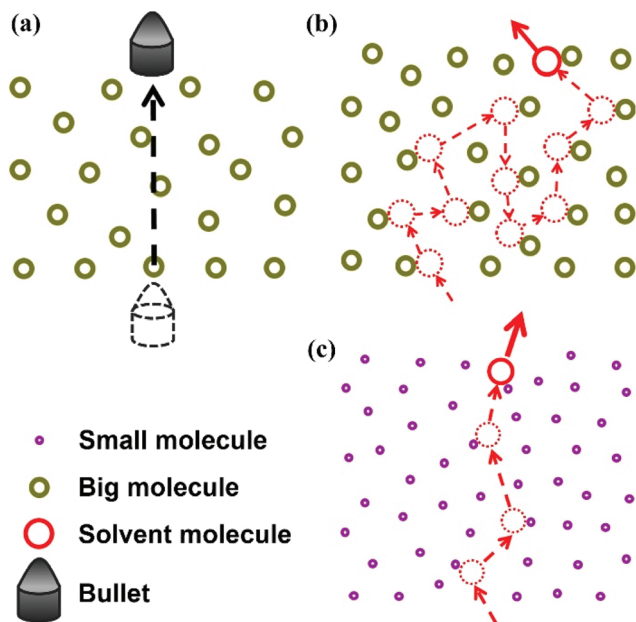

Fig. 2 Molecule collision analyzation: (a) a bullet flying, (b) solvent molecule colliding with a nitrogen molecule, and (c) solvent molecule colliding with a helium molecule.
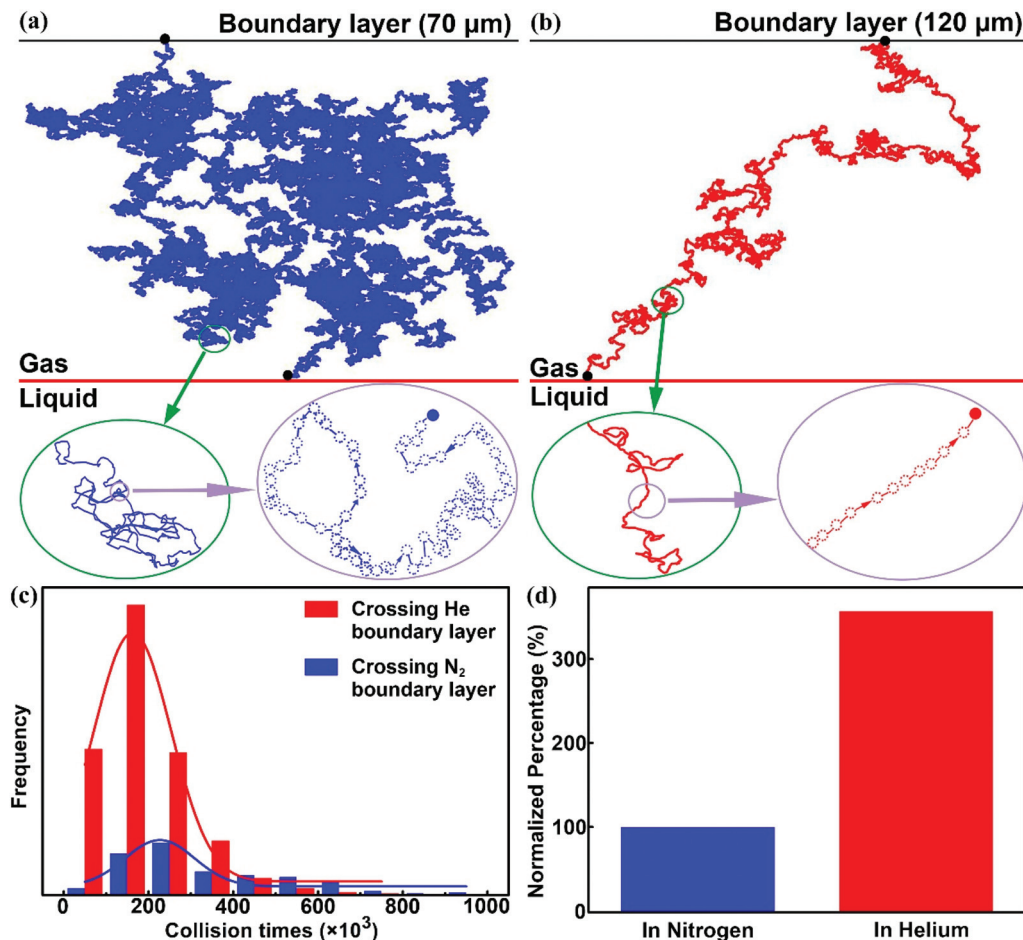
Fig. 3 Simulation statistical results of the collision between SMs and GMs. The collision route of SMs in the nitrogen (a) and the helium (b) boundary layer, respectively, (c) the collision times distribution between SMs and GMs, and (d) the proportion of SM numbers out of the boundary layer.

in Fig. 3d. The SM number crossing the helium boundary layer is nearly four times of the SM number crossing the nitrogen boundary layer. It can be concluded that solvent evaporates more quickly when drying by helium than by nitrogen.

All the abovementioned results illustrate that SMs can easily cross the thicker helium boundary layer, while it is difficult for SMs to cross the thin nitrogen boundary layer. The number of SMs out of the helium boundary layer is nearly four times that of the nitrogen boundary layer, and the collision times is much lower in the thicker helium boundary layer than in thin nitrogen boundary layer. Therefore, we can conclude that drying a liquid perovskite film by helium is much faster than by nitrogen.

Dependence of perovskite film properties on the drying gas

Based on the former simulation statistical results, the evaporation rate of perovskite film drying by helium is much faster than by nitrogen. In order to certify the results, we conducted experiments in which a liquid perovskite film was dried by helium and nitrogen, respectively. To compare two types of gas air-flow directly, we define Q as the air flow value at working condition ($P = 1.013 \times 10^5$ Pa, $T = 293$ K).

First, we optimized the best air flow value of nitrogen, as shown in Fig. 4. The drying of perovskite films by nitrogen presents dendrite grains and pin-holes morphology until an air flow value of 475 LPM. When Q is 110 LPM, the grain size can be up to several micrometers and the crisscrossed dendrites form some pin-hole, with a size of several micrometers, as shown in Fig. 4a. Subsequently, when Q increases to 260 LPM, the size of the perovskite dendrite gains is reduced and the pin-holes are tightly arranged, which is adverse to the perovskite solar cell, as shown in Fig. 4b. Until Q increases to 475 LPM, the film forms a compact morphology without the pin-hole, as shown in Fig. 4c. As we previously reported, more air flow can increase the liquid film crinkle. Therefore, 475 LPM is the optimized value that can achieve a compact film without excess. Furthermore, the optimized perovskite film was measured by AFM for surface roughness, as shown in Fig. 4d; the RMS of perovskite film drying by nitrogen is 10.23 nm at the random area of 10×10 μm^2, which is comparably uniform with even small scanning area.[20,38,39] Moreover, increasing Q continually is not a smart way because of the arousing solution film wave.[33]
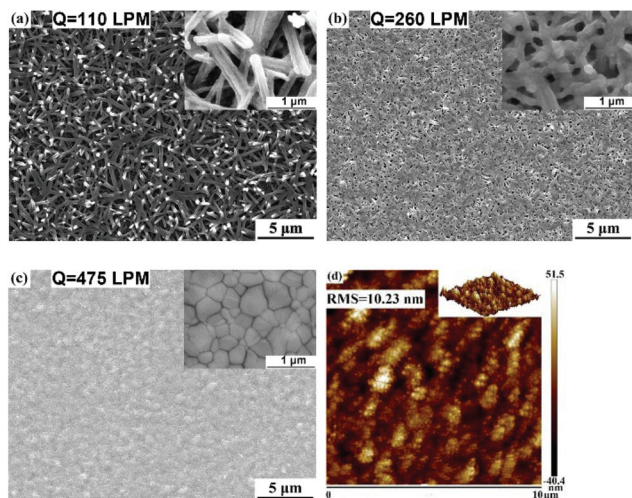
Fig. 4 (a–c) SEM morphologies of perovskite film drying by nitrogen at 110, 260, and 475 LPM, respectively; (d) AFM morphologies of perovskite film drying at 475 LPM by nitrogen.

In addition, we set Q as 105, 140, and 170 LPM to dry the perovskite film by helium, as shown in Fig. 5. It is worth noting that a perovskite film can achieve a compact and pin-hole free morphology only by 140 LPM helium at the same condition, whereas nitrogen needs at least 475 LPM. Even if Q is 105 LPM of helium, there are only several tiny pin-holes on the film, as shown in Fig. 5a. It can be accounted that solvent molecules cannot be completely removed in a short time. Moreover, when Q of helium is 140 LPM or larger, the film morphology is absolutely compact, as shown in Fig. 5b and c. In addition, the AFM morphology of perovskite film drying by 140 LPM is shown in Fig. 5d. The RMS is 8.56 nm at the random area of $10 \times 10 \ \mu m^2$, which is smoother than that of a film dried by nitrogen. In addition, increasing Q can achieve a
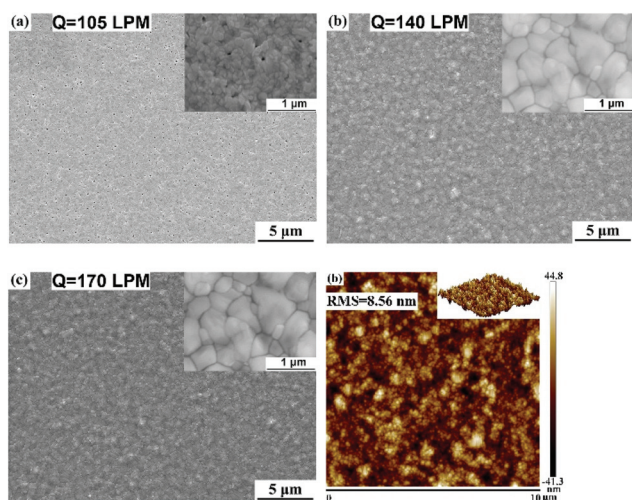

Fig. 5 (a–c) SEM morphologies of perovskite film drying by helium at 105, 140, and 170 LPM, respectively; (d) AFM morphologies of perovskite film drying at 140 LPM by helium.

void-free perovskite film but wastes gases. Therefore, a lower air flow of helium can achieve a compact and smooth perovskite film.

In summary, it can be concluded that a perovskite film can achieve a compact morphology with a small amount of helium, of which the usage is 0.29 of nitrogen. The experiment result is well consistent with that by Monte Carlo simulation which reveals the number of SMs out of the nitrogen boundary layer is 28% of helium boundary layer. It can be noted that small helium molecules would not significantly change the SMs' diffusion direction. They can drive SMs' diffusion quickly. Subsequently, solvent evaporation is faster. Therefore, drying liquid perovskite film by helium is much faster than by nitrogen, and the usage of helium is much less than nitrogen.

Device performance

To demonstrate that our pore-free $CH_3NH_3PbI_3$ ($MAPbI_3$) film would be an efficient light harvester for solar cells, we prepared a simple device structure using typical TiO_2 as electron transport layers (ETL) and spiro-OMeTAD as a hole transport layer (HTL). The device planar heterojunction structure is displayed in Fig. 6a. Perovskite films were dried by nitrogen with optimized air flow (475 LPM), and helium with the lowest air flow (140 LPM), which can achieve a compact morphology.

Fig. 6b shows the J–V cures of the typical devices. The power conversion efficiency (PCE) of the helium drying film-based device is 18.440% with an open circuit voltage (V_{oc}) of 1.094 V, short circuit current density (J_{sc}) of 22.717 mA cm^{-2} and fill factor (FF) of 0.742. The nitrogen drying film-based device achieved a slightly lower efficiency of 17.613%, with a relatively lower V_{oc} of 1.085 V, J_{sc} of 22.298 mA cm^{-2} and FF of 0.728. We attribute the electrical performance difference to the more compact perovskite films. Furthermore, the devices were measured with different scanning direction and rates, as shown in Fig. S2a.† The steady state PCEs of helium- and nitrogen-based devices were measured at its maximum power point as a function of time at the forward bias 0.881 and 0.862 V, respectively. Device efficiency was reduced slightly because of the hysteresis effect, as shown in Fig. S2b and c.† In addition, the devices have highly reproducibility. The statistical distribution of photovoltaic parameters on 40 devices is shown in Fig. 6c, and the average photovoltaic parameters are summarized in Table S3.† Basically, the parameters of helium-based devices are better than nitrogen-based devices because of the excellent perovskite films.

In spite of the high photovoltaic efficiency, one major concern is whether perovskite solar cells are durable enough for terrestrial applications.[5,40,41] We therefore investigated the stability of devices incorporating the pore-free perovskite absorbers. All cells without encapsulation were tested in ambient air (30% ± 5% humidity; 20 ± 5 °C) and stored in a drying oven without measuring the stability, as shown in Fig. 6d. In terms of PCE, the helium drying film-based device can be retained for more than 1000 hours with about 90% original efficiency. Even the device based on nitrogen drying film can retain 80% original efficiency. This illustrates that a
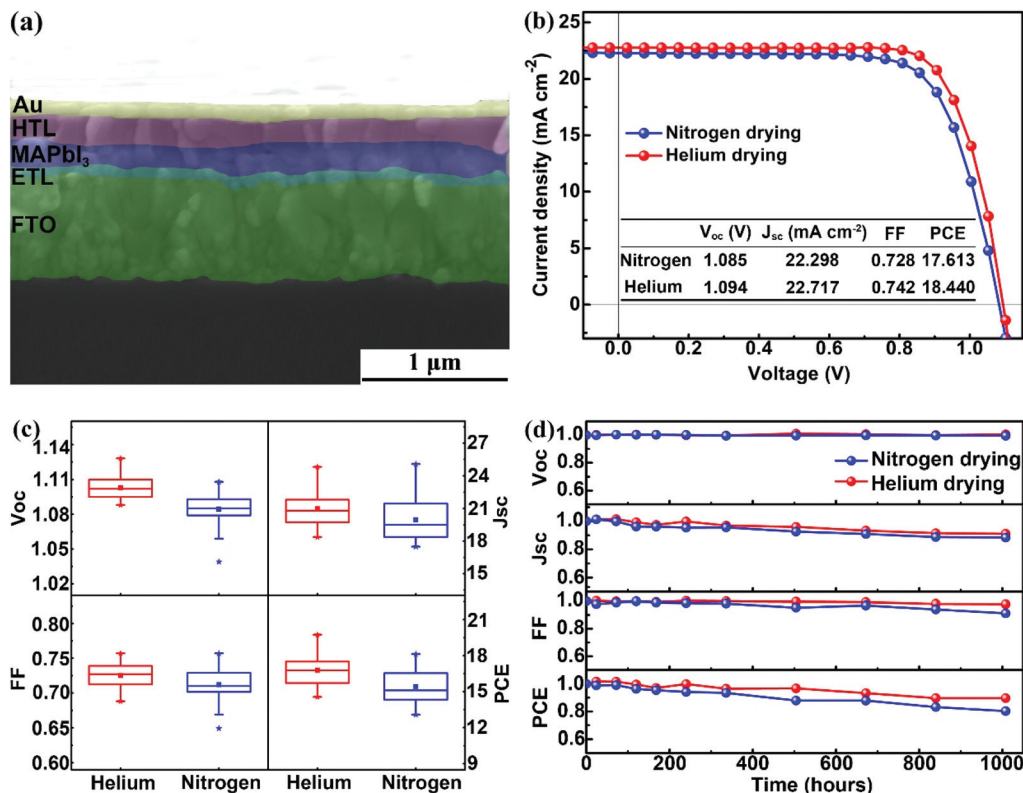
Fig. 6 (a) Structure of the planar heterojunction perovskite solar cells, (b) J–V curves of the solar cells employing perovskite film drying by nitrogen and helium, (c) statistical distribution of photovoltaic parameters extracted from J–V measurements of 40 number devices under simulated AM 1.5 (100 mW cm^{-2}) illumination; the data are represented as a standard box plot with V_{oc}, J_{sc}, FF, and PCE, and (d) stability of a device in an ambient environment without encapsulation.

more compact perovskite film is favourable for device lifetime because of the difficult decomposition.[40] The degradation of key photovoltaic parameters, *i.e.*, J_{sc}, V_{oc} and FF *versus* time, is also summarized. It is worth noting that V_{oc} is almost about 1.10 V showing little degradation. J_{sc} declines to about 86% of the original. FF shows different degradation for two types of devices. FF of the helium drying film-based device is stable all the time, whereas FF of the nitrogen drying film-based device declines to 90% of the original. Therefore, we can conclude from the above that a more compact perovskite film is favourable for device stability. The decay of the devices is mainly aroused by the decomposition of perovskite films, resulting from moisture or temperature.[5] Thereby, devices were further measured and stored directly at a more strict ambient environment. As shown in Fig. S3 and S4,† devices without any encapsulation degraded more seriously with an increase in humidity and temperature.

results show that the number of SMs out of the helium boundary layer is nearly four times that of the nitrogen boundary layer, and the collision times with helium molecules are much lower than nitrogen molecules. SMs' collision with helium molecules in the helium boundary layer presents a directed outside phenomenon, which significantly promotes solvent evaporation, while collision with nitrogen molecules is quite complex and circuitous. Moreover, the experimental results show that a fully compact and smooth perovskite film is easily achieved by drying with helium with less usage. We applied this helium-drying-based light absorber in a planar hetero-junction structure solar cell for the initial trial and achieved a power conversion efficiency of 18.44%. Our device also shows excellent enduring stability in ambient environment; it maintains 90% of the original efficiency after more than 1000 hours. The reason can be attributed to the compact perovskite film. The small helium-driven directed diffusion movement provides a promising solvent engineering fast perovskite film precipitation.

Conclusions

In the present study, we explored, for the first time, a small molecule (helium) driving directed diffusion movement in the boundary layer, which significantly promotes fast precipitation of pin-hole free perovskite film. The Monte Carlo simulation

Conflicts of interest

The authors declare no competing financial interest.

Acknowledgements

Notes and references

1 W. S. Yang, J. H. Noh, N. J. Jeon, Y. C. Kim, S. Ryu, J. Seo and S. I. Seok, *Science*, 2015, **348**, 1234–1237.

2 D. Q. Bi, W. Tress, M. I. Dar, P. Gao, J. S. Luo, C. Renevier, K. Schenk, A. Abate, F. Giordano, J. P. C. Baena, J. D. Decoppet, S. M. Zakeeruddin, M. K. Nazeeruddin, M. Gratzel and A. Hagfeldt, *Sci. Adv.*, 2016, **2**, e1501170.

3 H. Zhang, X. F. Qiao, Y. Shen, T. Moehl, S. M. Zakeeruddin, M. Gratzel and M. K. Wang, *J. Mater. Chem. A*, 2015, **3**, 11762–11767.

4 D. Bi, C. Yi, J. Luo, J.-D. Décoppet, F. Zhang, S. M. Zakeeruddin, X. Li, A. Hagfeldt and M. Grätzel, *Nat. Energy*, 2016, **1**, 16142.

5 F. Zhang, W. D. Shi, J. S. Luo, N. Pellet, C. Y. Yi, X. Li, X. M. Zhao, T. J. S. Dennis, X. G. Li, S. R. Wang, Y. Xiao, S. M. Zakeeruddin, D. Q. Bi and M. Gratzel, *Adv. Mater.*, 2017, **29**, 1606806.

6 D. Shi, V. Adinolfi, R. Comin, M. J. Yuan, E. Alarousu, A. Buin, Y. Chen, S. Hoogland, A. Rothenberger, K. Katsiev, Y. Losovyj, X. Zhang, P. A. Dowben, O. F. Mohammed, E. H. Sargent and O. M. Bakr, *Science*, 2015, **347**, 519–522.

7 M. Saliba, T. Matsui, J.-Y. Seo, K. Domanski, J.-P. Correa-Baena, M. K. Nazeeruddin, S. M. Zakeeruddin, W. Tress, A. Abate and A. Hagfeldt, *Energy Environ. Sci.*, 2016, **9**, 1989–1997.

8 S. D. Stranks, G. E. Eperon, G. Grancini, C. Menelaou, M. J. P. Alcocer, T. Leijtens, L. M. Herz, A. Petrozza and H. J. Snaith, *Science*, 2013, **342**, 341–344.

9 J. Burschka, N. Pellet, S. J. Moon, R. Humphry-Baker, P. Gao, M. K. Nazeeruddin and M. Gratzel, *Nature*, 2013, **499**, 316–319.

10 E. Nouri, M. R. Mohammadi and P. Lianos, *Chem. Commun.*, 2017, **53**, 1630–1633.

11 J. Du, Z. Du, J. S. Hu, Z. Pan, Q. Shen, J. Sun, D. Long, H. Dong, L. Sun, X. Zhong and L. J. Wan, *J. Am. Chem. Soc.*, 2016, **138**, 4201–4209.

12 K. A. Bush, A. F. Palmstrom, Z. J. Yu, M. Boccard, R. Cheacharoen, J. P. Mailoa, D. P. McMeekin, R. L. Z. Hoye, C. D. Bailie, T. Leijtens, I. M. Peters, M. C. Minichetti, N. Rolston, R. Prasanna, S. Sofia, D. Harwood, W. Ma, F. Moghadam, H. J. Snaith, T. Buonassisi, Z. C. Holman, S. F. Bent and M. D. McGehee, *Nat. Energy*, 2017, **2**, 17009.

13 N. Wang, Y. Y. Zhou, M. G. Ju, H. F. Garces, T. Ding, S. P. Pang, X. C. Zeng, N. P. Padture and X. W. Sun, *Adv. Energy Mater.*, 2016, **6**, 1601130.

14 R. Dong, Y. J. Fang, J. Chae, J. Dai, Z. G. Xiao, Q. F. Dong, Y. B. Yuan, A. Centrone, X. C. Zeng and J. S. Huang, *Adv. Mater.*, 2015, **27**, 1912–1918.

15 M. D. Xiao, F. Z. Huang, W. C. Huang, Y. Dkhissi, Y. Zhu, J. Etheridge, A. Gray-Weale, U. Bach, Y. B. Cheng and L. Spiccia, *Angew. Chem., Int. Ed.*, 2014, **53**, 9898–9903.

16 G. E. Eperon, V. M. Burlakov, P. Docampo, A. Goriely and H. J. Snaith, *Adv. Funct. Mater.*, 2014, **24**, 151–157.

17 M. Z. Liu, M. B. Johnston and H. J. Snaith, *Nature*, 2013, **501**, 395–398.

18 Y. Yu, S. W. Yang, L. Lei and Y. Liu, *Nanoscale*, 2017, **9**, 2569–2578.

19 M. Zhang, H. Yu, J. H. Yun, M. Q. Lyu, Q. Wang and L. Z. Wang, *Chem. Commun.*, 2015, **51**, 10038–10041.

20 N. J. Jeon, J. H. Noh, Y. C. Kim, W. S. Yang, S. Ryu and S. I. Seok, *Nat. Mater.*, 2014, **13**, 897–903.

21 L.-L. Gao, L.-S. Liang, X.-X. Song, B. Ding, G.-J. Yang, B. Fan, C.-X. Li and C.-J. Li, *J. Mater. Chem. A*, 2016, **4**, 3704–3710.

22 Z. M. Zhou, Z. W. Wang, Y. Y. Zhou, S. P. Pang, D. Wang, H. X. Xu, Z. H. Liu, N. P. Padture and G. L. Cui, *Angew. Chem., Int. Ed.*, 2015, **54**, 9705–9709.

23 Y. Zhou, M. Yang, W. Wu, A. L. Vasiliev, K. Zhu and N. P. Padture, *J. Mater. Chem. A*, 2015, **3**, 8178–8184.

24 W. D. Zhu, T. Yu, F. M. Li, C. X. Bao, H. Gao, Y. Yi, J. Yang, G. Fu, X. X. Zhou and Z. G. Zou, *Nanoscale*, 2015, **7**, 5427–5434.

25 V. O. Eze, B. Lei and T. Mori, *Jpn. J. Appl. Phys.*, 2016, **55**, 02BF08.

26 B. Xia, Z. X. Wu, H. Dong, J. Xi, W. Wu, T. Lei, K. Xi, F. Yuan, B. Jiao, L. X. Xiao, Q. H. Gong and X. Hou, *J. Mater. Chem. A*, 2016, **4**, 6295–6303.

27 F. Z. Huang, Y. Dkhissi, W. C. Huang, M. D. Xiao, I. Benesperi, S. Rubanov, Y. Zhu, X. F. Lin, L. C. Jiang, Y. C. Zhou, A. Gray-Weale, J. Etheridge, C. R. McNeill, R. A. Caruso, U. Bach, L. Spiccia and Y. B. Cheng, *Nano Energy*, 2014, **10**, 10–18.

28 Y. Dkhissi, F. Huang, S. Rubanov, M. Xiao, U. Bach, L. Spiccia, R. A. Caruso and Y.-B. Cheng, *J. Power Sources*, 2015, **278**, 325–331.

29 J. Kim, J. S. Yun, X. Wen, A. M. Soufiani, C. F. J. Lau, B. Wilkinson, J. Seidel, M. A. Green, S. Huang and A. W. Y. Ho-Baillie, *J. Phys. Chem. C*, 2016, **120**, 11262–11267.

30 S. Razza, F. Di Giacomo, F. Matteocci, L. Cinà, A. L. Palma, S. Casaluci, P. Cameron, A. D'Epifanio, S. Licoccia, A. Reale, T. M. Brown and A. Di Carlo, *J. Power Sources*, 2015, **277**, 286–291.

31 K. Hwang, Y. S. Jung, Y. J. Heo, F. H. Scholes, S. E. Watkins, J. Subbiah, D. J. Jones, D. Y. Kim and D. Vak, *Adv. Mater.*, 2015, **27**, 1241–1247.

32 S. Song, M. T. Horantner, K. Choi, H. J. Snaith and T. Park, *J. Mater. Chem. A*, 2017, **5**, 3812–3818.

33 L. L. Gao, C. X. Li, C. J. Li and G. J. Yang, *J. Mater. Chem. A*, 2017, **5**, 1548–1557.

34 R. L. Daugherty and A. C. Ingersoll, *Fluid mechanics*, McGraw-Hill, 1954.

35 N. Li, H. P. Dong, H. Dong, J. L. Li, W. Z. Li, G. D. Niu, X. D. Guo, Z. X. Wu and L. D. Wang, *J. Mater. Chem. A*, 2014, **2**, 14973–14978.

36 H. Schlichting and K. Gersten, *Fluid Mech.*, 2017, **20**, 48–89.

37 H. Schlichting and K. Gersten, in *Boundary-Layer Theory*, Springer, 2017, pp. 29–49.

38 D. Yang, Z. Yang, W. Qin, Y. L. Zhang, S. Z. Liu and C. Li, *J. Mater. Chem. A*, 2015, **3**, 9401–9405.

39 F. X. Xie, D. Zhang, H. Su, X. Ren, K. S. Wong, M. Grätzel and W. C. Choy, *ACS Nano*, 2015, **9**, 639–646.

40 J. B. You, L. Meng, T. B. Song, T. F. Guo, Y. Yang, W. H. Chang, Z. R. Hong, H. J. Chen, H. P. Zhou, Q. Chen, Y. S. Liu, N. De Marco and Y. Yang, *Nat. Nanotechnol.*, 2016, **11**, 75–82.

41 B. Lee, C. C. Stoumpos, N. Zhou, F. Hao, C. Malliakas, C. Y. Yeh, T. J. Marks, M. G. Kanatzidis and R. P. Chang, *J. Am. Chem. Soc.*, 2014, **136**, 15379–15385.